Characterization of cores from an *in-situ* recovery mined uranium deposit in Wyoming: Implications for post-mining restoration

G. WoldeGabriel [a,*], H. Boukhalfa [a], S.D. Ware [a], M. Cheshire [a], P. Reimus [a], J. Heikoop [a], S.D. Conradson [b], O. Batuk [a], G. Havrilla [c], B. House [a], A. Simmons [a], J. Clay [d], A. Basu [e], J.N. Christensen [e], S.T. Brown [e], D.J. DePaolo [e]

[a] Earth and Environmental Sciences Division, Los Alamos National Laboratory, Los Alamos, NM 87545, USA
[b] Materials Science and Technology Division, Los Alamos National Laboratory, Los Alamos, NM 87545, USA
[c] C-CDE: Chemical Diagnostics and Engineering, Los Alamos National Laboratory, Los Alamos, NM 87545, USA
[d] Cameco Resources Inc., 2020 Carey Avenue, Suite 600, Cheyenne, WY 82001, USA
[e] Center for Isotope Geochemistry, Department of Earth and Planetary Science, UC Berkeley, Berkeley, CA 94720-4767, USA

ARTICLE INFO

ABSTRACT

In-situ recovery (ISR) of uranium (U) from sandstone-type roll-front deposits is a technology that involves the injection of solutions that consist of ground water fortified with oxygen and carbonate to promote the oxidative dissolution of U, which is pumped to recovery facilities located at the surface that capture the dissolved U and recycle the treated water. The ISR process alters the geochemical conditions in the subsurface creating conditions that are more favorable to the migration of uranium and other metals associated with the uranium deposit. There is a lack of clear understanding of the impact of ISR mining on the aquifer and host rocks of the post-mined site and the fate of residual U and other metals within the mined ore zone. We performed detailed petrographic, mineralogical, and geochemical analyses of several samples taken from about 7 m of core of the formerly the ISR-mined Smith Ranch–Highland uranium deposit in Wyoming. We show that previously mined cores contain significant residual uranium (U) present as coatings on pyrite and carbonaceous fragments. Coffinite was identified in three samples. Core samples with higher organic (>1 wt.%) and clay (>6–17 wt.%) contents yielded higher $^{234}U/^{238}U$ activity ratios (1.0–1.48) than those with lower organic and clay fractions. The ISR mining was inefficient in mobilizing U from the carbonaceous materials, which retained considerable U concentrations (374–11,534 ppm). This is in contrast with the deeper part of the ore zone, which was highly depleted in U and had very low $^{234}U/^{238}U$ activity ratios. This probably is due to greater contact with the lixiviant (leaching solution) during ISR mining.

EXAFS analyses performed on grains with the highest U and Fe concentrations reveal that Fe is present in a reduced form as pyrite and U occurs mostly as U(IV) complexed by organic matter or as U(IV) phases of carbonate complexes. Moreover, U–O distances of ~2.05 Å were noted, indicating the potential formation of other poorly defined U(IV/VI) species. We also noted a small contribution from U═O at 1.79 Å, which indicates that U is partially oxidized. There is no apparent U–S or U–Fe interaction in any of the U spectra analyzed. However, SEM analysis of thin sections prepared from the same core material reveals surficial U associated with pyrite which is probably a minor fraction of the total U present as thin coatings on the surface of pyrite.

Our data show the presence of different structurally variable uranium forms associated with the mined cores. U associated with carbonaceous materials is probably from the original U mobilization that accumulated in the organic matter-rich areas under reducing conditions during shallow burial diagenesis. U associated with pyrite represents a small fraction of the total U and was likely deposited as a result of chemical reduction by pyrite. Our data suggest that areas rich in carbonaceous materials had limited exposure to the lixiviant solution, continue to be reducing, and still hold significant U resources. Because of their limited access to fluid flow, these areas might not contribute significantly to post-mining U release or attenuation. Areas with pyrite that are accessible to fluids seem to be more reactive and could act as reductants and facilitate U reduction and accumulation, limiting its migration.

1. Introduction

The sandstone-type roll-front deposits located in the southern part of the Powder River Basin in Wyoming host the largest *in-situ* recovery

* Corresponding author. Tel.: +1 505 667 8749.
E-mail address: wgiday@lanl.gov (G. WoldeGabriel).

(ISR) operation in the United States, the Smith Ranch–Highland facility, presently operated by Cameco Resources (Fig. 1) (Flores et al., 1999; Freeman and Stover, 1999). The principal U minerals associated with arkosic sandstone beds were identified as pitchblende and coffinite, and in most cases occur with pyrite, marcasite, hematite, ferroselite, native selenium, and calcite (Dahlkamp, 1993; Stewart et al., 2000; Heinrich, 2012). U was derived from multiple sources, including granitic rocks located to the south of the Powder River Basin and from the alteration and leaching of granitic sediments and late Tertiary volcanic ashes deposited in the area. The U subsequently migrated in oxygen- and carbonate-rich waters until it encountered an oxidation–reduction interface within organic-rich and organic-poor arkosic sandstone units, where it formed roll-front ore zones (Seeland, 1976; Santos, 1981; Freeman and Stover, 1999; Norris and Drummond, 2000). ISR is a solution mining technique that involves the injection of oxygen- and CO_2-fortified water (Miller et al., 1990; Norris and Drummond, 2000) to economically extract U from low-grade ore deposits while avoiding the production of tailings and U-bearing dust associated with conventional open-pit and/or underground mining operations. The main challenges with ISR mining are the inability to access all of the U in the ore zone, and, more importantly, the difficulties in restoring groundwater to baseline conditions and the mined host rocks to chemically reducing conditions capable of immobilizing any residual U or other contaminants.

During ISR mining, U(IV) minerals are oxidized to form highly soluble uranyl hydroxycarbonate species ($UO_2(CO_3)_n(OH)_m^{2-2n-m}$) or calcium–uranyl–carbonate species ($CaUO_2(CO_3)_n^{4-2n}$), which is facilitated by the presence of excess carbonate. The U(VI)-rich solutions are pumped to the surface for U recovery using ion-exchange methods. Following ISR mining, restoration is typically conducted by sweeping the mined ore body with aquifer water drawn in from outside the ore zone (groundwater sweep) and then treating the ore zone water by reverse osmosis (RO). Treatment with reducing agents (H_2, Na_2S and H_2S) has also been used to restore the reducing capacity of the aquifer in an attempt to reverse the oxidizing conditions created during ISR mining (Mays, 1994; Hall, 2009). Bioremediation, through the stimulation of native metal reducing bacteria within the aquifer has also been considered for the restoration of mined sites (Mays, 1994; Reimann and Huffman, 2005; Luo et al., 2007; Hall, 2009; Yi et al., 2009; Hu et al., 2011). An understanding of the chemical speciation of U in postmined ore material and of the nature of associated minerals and geochemical conditions would help in evaluating and applying these and other remediation strategies.
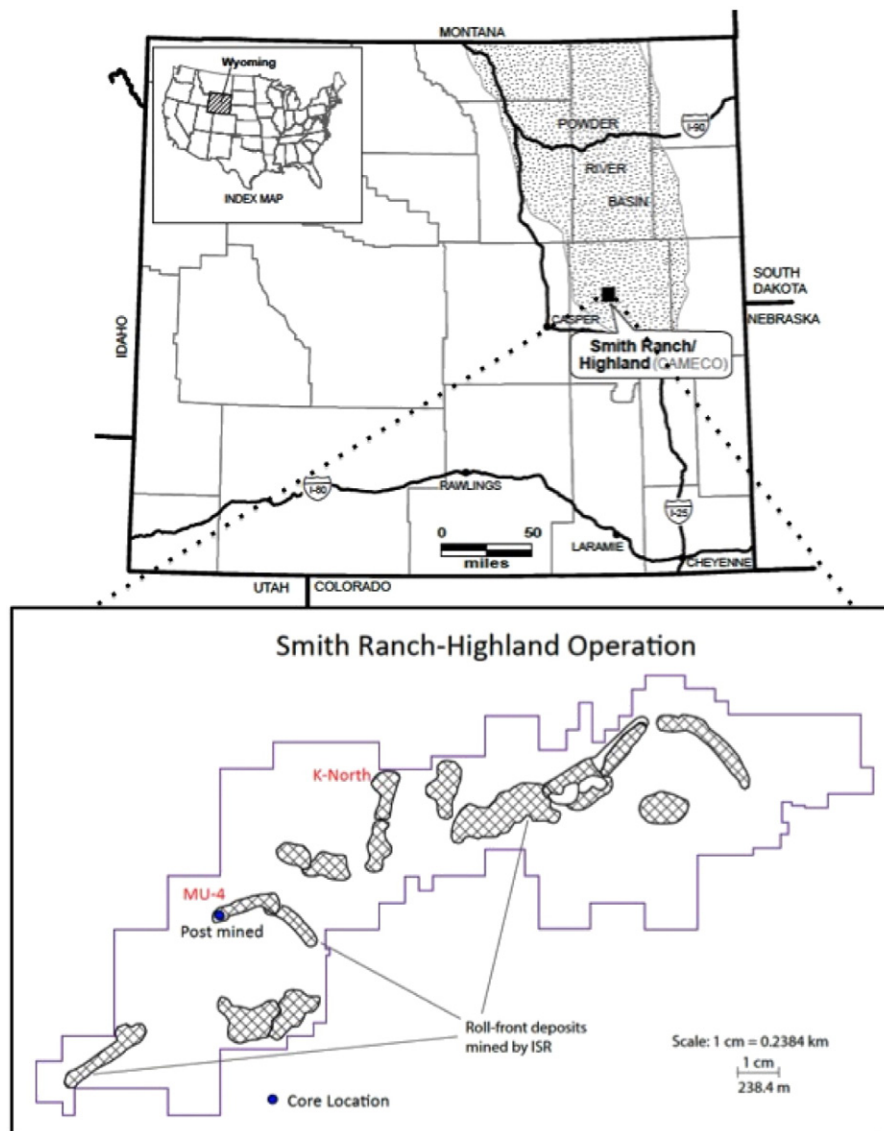

Fig. 1. Map showing the location of the Smith Ranch–Highland mining site and the core hole (Easting 348,744.59 ft, Northing 867,055.62 ft, elevation 5456.81 ft, and water level at 259.3 ft) at mine unit (MU)-4 in the southern part of the Powder River Basin in east-central Wyoming.

Although considerable work has been done to characterize U-bearing deposits prior to mining (Stewart et al., 2000; Heinrich, 2012), information is sparse on previous studies investigating how roll-front sediments are affected by ISR mining, a key factor governing post-mining behavior of U. For this study, post-mining core samples were obtained from mining unit (MU)-4 at the Smith Ranch–Highland U deposit in Wyoming (Fig. 1), which was mined by ISR methods from 1999 to 2005 and was designated as being 'in restoration' starting in 2010. The goals of the study were to conduct detailed characterizations of the core sample sediments, with emphasis on identifying and evaluating mining signatures that might be exploited to improve or assess restoration methods and also to evaluate whether the sediments retain some capacity to reduce U(VI) and thus prevent significant U migration out of the previously mined areas. An additional benefit of the study was to gain insights into the efficiency of hydrologic sweep of the lixiviant solution during mining, as reflected by the spatial distribution of geochemical and isotopic signatures in the core samples. Specific tools that we employed included optical petrography, scanning electron microscopy (SEM), total organic carbon analysis, U and strontium (Sr) concentration and isotopic measurements of strong acid leachates of selected samples to assess ISR fluid–rock interactions, and X-ray diffraction, X-ray absorption and X-ray fluorescence measurements (see below for details) on selected solid samples to determine U and Fe structures, oxidation states, speciation, and mineral associations in the sediments. Understanding the structure and chemical speciation of U and associated minerals in post-mined ore deposits will help define the geochemical environments that exist in the subsurface after ISR mining, thus providing insights into conditions and processes responsible for the continued release of U and other trace metals from previously mined zones, which in turn should help in developing more robust restoration methods.

2. Materials and methods

2.1. Core selection and analytical techniques

Cameco Resources provided six vacuum-packed 0.3 m (one-foot) sections of a 7.32 m (~24 ft) continuous core of semi-consolidated light to medium gray arkosic sandstone from the Smith Ranch–Highland MU-4 site (Fig. 1), which was mined from 1999 to 2005 and is currently in the process of being restored using groundwater sweep and reverse osmosis (Clay, Personal communication, 2013). The post-ISR samples were selected from different levels of the ore zone located between 233.5 and 239.6 m below the ground surface. Even though most of the samples exhibit generally similar petrographic, mineralogical, and chemical properties and generally contain proportional amounts of organic matter, U, and pyrite (Tables 1–3), the detailed characterization work reported in this paper was conducted on an organic-rich subsample of core from 237.4 m depth (designated as "779 dark") because of its high organic content, which contained considerably more uranium compared with the other core samples (Tables 2 and 3).

Subsamples of the core were selected and processed for thin sections and for quantitative X-ray diffraction (QXRD), and X-ray fluorescence (XRF) measurements. The depths and identifiers of the samples prepared for this study are listed in Table 1. These samples were also analyzed for total organic carbon content, and they were acid leached to analyze U and Sr isotopes in the leachates. X-ray absorption near edge spectroscopy (XANES) and extended X-ray absorption fine structure (EXAFS) analyses were also performed on selected thin sections.

2.2. Optical and scanning electron microscope studies

Thin sections of post-mined core samples (n = 15) were prepared in epoxy resin and heated to accelerate hardening. No special precautions were taken to minimize contact between the samples and air during thin section preparation. Thin sections were examined under transmitted, polarized, and reflected light using optical microscopy to determine

Table 1

Mineralogical compositions of core samples from the Smith Ranch–Highland uranium deposit mining unit 4 in Wyoming. Concentrations are given in wt.%.

Samples	766-1	766-2	767-1	769 dark	769-1	769-2	770-1	779 dark
Depth (m)	233.5	233.6	233.8	234.4	234.5	234.7	234.6	237.6
Quartz	63.1	66.4	61.7	58.6	54.4	59.3	59.8	35.6
Albite	3.0	2.9	1.9	3.6	3.2	8.2	7.2	c
K-feldspar	14.7	15.0	16.3	24.0	20.4	21.1	22.4	43.8
Muscovite	2.5	3.5	2.9	3.6	4.9	3.5	2.2	c
Kaolinite	2.1	2.6	2.8	1.2	2.4	2.2	1.9	2.1
Calcite	a	c.	a	0.6	c	a	0.7	c
Smectite	13.7	9.3	13.9	6.0	14.2	4.2	5.8	12.3
Pyrite	a	a	a	2.4	0.5	1.0	c	6.2
Coffinite	c	c	c	b	c	c	c	b
Total	100	100	100	100	100	100	100	100

Samples	779-1	779-2	780-1	782c	782-2	785-1	786-1
Depth (m)	237.4	237.6	237.7	238.4	238.7	239.3	239.6
Quartz	55.5	58.5	60.2	72.7	71.1	59.3	68.9
Albite	2.7	4.9	7.9	4.7	5.9	10.3	3.7
K-feldspar	20.9	16.4	24.6	11.3	12.2	13.3	15.9
Muscovite	2.9	10.7	1.5	3.1	2.7	4.4	2.8
Kaolinite	2.9	1.6	1.5	1.9	2.0	2.9	1.6
Calcite	a	c	a	a	0.6	a	0.6
Smectite	14.4	6.6	4.0	6.0	5.5	9.5	6.6
Pyrite	0.5	1.3	c	c	c	c	c
Coffinite	c	b	c	c	c	c	c
Total	100	100	100	100	100	100	100

a, concentrations less than 0.5 wt.%.
b, present but could not quantify due to lack of standard.
c, below detection limits.

the detrital and secondary minerals and the textural features of the U-mineralized rocks (Fig. 2). At least three thin sections and several fragments from each sample were also examined using scanning electron microscopy (SEM). The SEM images and spectral patterns from EDX (energy dispersive X-ray) analysis were used to identify the detrital and secondary mineral phases and to investigate the distributions, morphologies, and the paragenetic relations of the clays, carbonaceous matter, U minerals, and pyrite (Figs. 2–4).

2.3. Quantitative X-ray diffraction

Representative fragments were taken from each of the cores for full-pattern quantitative X-ray diffraction (QXRD) analyses. All samples (n = 15) and standards were spiked with 20 wt.% Al_2O_3 (metallurgical-grade Al_2O_3) and ground under acetone with a Retsch mortar and pestle to a particle size <5 μm. The samples were loaded into a front-loading Ti mount. X-ray analyses were run from 2 to 70° 2θ scan rate of 8–12 s/step with Cu-Kα radiation. Mineral identification and unit-cell parameters analysis was performed using the Jade© 7.5 X-ray data evaluation program with ICDD PDF-4 database. Quantitative phase analysis was performed using FULLPAT (Chipera and Bish, 2002). Mineralogical compositions of the core samples are presented in Table 1.

2.4. X-ray fluorescence spectroscopy

Aliquots from the powdered samples of cores prepared for the QXRD analyses were fused to prepare glass disks to determine the major and trace element compositions using a Rigaku Primus II wavelength-dispersive X-ray fluorescence (XRF) spectrometer. The samples (n = 15) were first crushed and homogenized in 5–10 g portions in a tungsten-carbide ball mill. Sample splits were heated at 110 °C for 4 h and then allowed to equilibrate at ambient laboratory conditions for 12 h. To prepare fusion disks, 1.25 gram splits were mixed with 8.75 g of lithium metaborate-tetraborate flux and heated in a muffle furnace

Table 2
Major, trace, and rare earth element compositions of arkosic sandstone cores from the Smith Ranch–Highland uranium deposit mining unit-4, Wyoming. Concentrations are given in wt.%.

Samples	Depth (m)	SiO₂	TiO₂	Al₂O₃	Fe₂O₃	MnO	MgO	CaO	Na₂O	K₂O	P₂O₅	Total	LOI
766-1	233.48	75.50	0.23	6.21	1.28	0.01	0.58	0.55	0.30	2.22	0.04	86.92	12.69
766-2	233.63	86.40	0.15	6.27	0.85	0.01	0.55	0.35	0.36	2.32	0.05	97.30	2.61
767-1	233.75	83.63	0.15	6.79	1.18	0.01	0.60	0.39	0.34	2.51	0.05	95.65	4.26
769 dark	234.39	73.05	0.15	5.24	2.19	0.01	0.47	0.55	0.31	1.98	0.06	83.99	15.68
769-1	234.48	85.04	0.16	5.82	1.15	0.01	0.48	0.36	0.26	2.12	0.05	95.45	4.45
769-2	234.70	86.07	0.15	6.31	0.79	0.01	0.47	0.35	0.41	2.46	0.05	97.05	2.86
770-1	234.64	82.30	0.14	7.37	0.90	0.01	0.48	0.45	0.54	3.16	0.05	95.37	4.52
779-1	237.44	76.22	0.42	10.20	2.49	0.01	1.04	0.74	0.14	2.09	0.06	93.43	6.50
779-2	237.62	79.23	0.28	7.00	2.50	0.01	0.65	0.50	0.31	1.83	0.10	92.41	7.20
780-1	237.74	84.91	0.13	7.25	0.98	0.01	0.51	0.33	0.61	2.62	0.05	97.38	2.52
782c	238.35	87.88	0.16	5.62	0.95	0.01	0.46	0.31	0.36	2.03	0.05	97.82	2.09
782-2	238.68	87.06	0.13	6.15	0.85	0.01	0.45	0.31	0.43	2.30	0.05	97.73	2.18
785-1	239.27	87.96	0.17	5.75	0.82	0.01	0.44	0.33	0.46	2.07	0.05	98.05	1.85
786-1	239.57	88.10	0.24	5.51	0.89	0.01	0.43	0.34	0.43	1.94	0.05	97.93	1.96

Samples	Depth (m)	V	Cr	Ni	Cu	Zn	Ga	Ge	As	Rb	Sr	Y	Zr
766-1	233.48	84.00	33.00	13.00	14.00	19.00	<7.50	<7.50	42.40	83.20	71.00	16.00	398.00
766-2	233.63	24.00	19.00	13.00	7.00	10.00	<7.50	9.70	87.10	73.20	65.00	10.00	142.00
767-1	233.75	35.00	24.00	14.00	10.00	25.00	<7.50	<7.50	34.80	72.20	71.00	10.00	134.00
769 dark	234.39	120.00	30.00	23.00	16.00	19.00	7.40	79.10	41.70	119.80	54.00	18.10	167.00
769-1	234.48	37.00	18.00	14.00	11.00	20.00	<7.50	86.80	20.40	77.70	60.00	11.80	155.00
769-2	234.70	17.00	17.00	11.00	8.00	10.00	<7.50	76.30	43.90	76.80	64.00	10.00	165.00
770-1	234.64	35.00	15.00	19.00	11.00	11.00	<7.50	146.40	75.70	105.20	72.00	11.00	160.00
779-1	237.44	82.00	51.00	28.00	18.00	54.00	12.60	79.10	<18.00	99.70	90.00	15.00	300.00
779-2	237.62	63.00	36.00	55.00	13.00	459.00	<7.50	113.10	96.90	315.50	69.30	37.80	520.00
780-1	237.74	31.00	13.00	11.00	9.00	28.00	8.20	<7.50	<18.00	93.30	62.00	10.00	97.00
782c	238.35	67.00	17.00	13.00	7.00	15.00	<7.50	15.30	<18.00	64.00	56.00	8.00	144.00
782-2	238.68	45.00	13.00	12.00	10.00	16.00	<7.50	<7.50	<18.00	70.00	62.00	7.00	89.00
785-1	239.27	39.00	17.00	11.00	11.00	18.00	<7.50	<7.50	<18.00	63.00	60.00	9.00	259.00
786-1	239.57	69.00	17.00	13.00	7.00	14.00	<7.50	<7.50	<18.00	59.00	59.00	15.00	410.00

Samples	Depth (m)	Nb	Ba	La	Ce	Pr	Nd	Sm	Gd	Tb	Dy	Ho	Er
766-1	233.48	10.50	451.00	22.20	27.70	<28.50	<19.80	<15.60	<14.40	<20.70	<14.40	<17.70	<16.50
766-2	233.63	11.90	462.00	<22.80	<26.4	<28.50	<19.80	<15.60	<14.40	<20.70	<14.40	<17.70	<16.50
767-1	233.75	7.70	485.00	<22.80	<26.4	<28.50	<19.80	<15.60	<14.40	<20.70	<14.40	<17.70	<16.50
769 dark	234.39	67.10	385.00	25.60	39.10	<28.50	<19.80	<15.60	<14.40	<20.70	<14.40	<17.70	<16.50
769-1	234.48	19.60	427.00	22.20	33.40	<28.50	<19.80	<15.60	<14.40	<20.70	<14.40	<17.70	<16.50
769-2	234.70	8.40	473.00	<22.80	<26.4	<28.50	<19.80	<15.60	<14.40	<20.70	<14.40	<17.70	<16.50
770-1	234.64	14.00	548.00	<22.80	<26.4	<28.50	<19.80	15.50	<14.40	<20.70	<14.40	<17.70	<16.50
779-1	237.44	28.00	448.00	28.10	56.20	<28.50	<19.80	<15.60	<14.40	<20.70	<14.40	<17.70	<16.50
779-2	237.62	235.60	352.00	56.30	86.30	<28.50	24.90	<15.60	54.60	<20.70	<14.40	<17.70	<16.50
780-1	237.74	14.00	463.00	<22.80	<26.4	<28.50	<19.80	<15.60	<14.40	<20.70	<14.40	<17.70	<16.50
782c	238.35	16.00	457.00	<22.80	34.20	<28.50	<19.80	<15.60	<14.40	<20.70	<14.40	<17.70	<16.50
782-2	238.68	13.00	506.00	<22.80	<26.4	<28.50	<19.80	<15.60	<14.40	<20.70	<14.40	<17.70	<16.50
785-1	239.27	11.00	430.00	<22.80	35.80	<28.50	<19.80	<15.60	<14.40	<20.70	<14.40	<17.70	<16.50
786-1	239.57	14.00	413.00	29.80	58.60	<28.50	<19.80	<15.60	<14.40	<20.70	<14.40	<17.70	<16.50

Samples	Depth (m)	Tm	Yb	Lu	Hf	Pb	Bi	Th	U
766-1	233.48	<14.40	<14.70	<12.00	14.40	22.00	<4.80	9.70	144.20
766-2	233.63	<14.40	<14.70	<12.00	<9.30	16.00	<4.80	<5.40	148.40
767-1	233.75	<14.40	<14.70	<12.00	<9.30	37.00	<4.80	<5.40	163.70
769 dark	234.39	<14.40	<14.70	<12.00	<9.30	4.00	<4.80	6.20	2569.70
769-1	234.48	<14.40	<14.70	<12.00	<9.30	22.00	<4.80	6.20	711.60
769-2	234.70	<14.40	<14.70	<12.00	<9.30	16.00	<4.80	<5.40	180.60
770-1	234.64	<14.40	<14.70	<12.00	<9.30	13.00	<4.80	<5.40	504.60
779-1	237.44	<14.40	<14.70	<12.00	22.90	28.00	<4.80	5.30	781.10
779-2	237.62	<14.40	<14.70	<12.00	10.20	15.00	<4.80	10.50	11,534.20
780-1	237.74	<14.4	<14.7	<12	<9.3	114.00	<4.8	5.30	374.00
782c	238.35	<14.4	<14.7	<12	<9.3	15.00	<4.8	<5.4	23.70
782-2	238.68	<14.4	<14.7	<12	<9.3	70.00	<4.8	<5.4	<5.4
785-1	239.27	<14.4	<14.7	<12	<9.3	23.00	<4.8	12.30	<5.4
786-1	239.57	<14.4	<14.7	<12	17.00	17.00	<4.8	8.80	<5.4

for 30 min at 1015 °C. Additional one-gram splits were heated at 1000 °C to obtain the loss on ignition (LOI) measurements to determine total volatile contents (i.e., H_2O, CO_2, F, Cl, S, etc.) in the samples in weight percentage and to be used in the data reduction program. Elemental concentrations were calculated by comparing X-ray intensities for the samples to those for 17 standards of known composition using "consensus values" from Govindaraju, 1994. Intensities were reduced using the de Jongh model empirical method to calculate

theoretical matrix correction coefficients (Rigaku Corporation, 2009). Results are presented in Table 2.

2.5. Organic carbon analysis

The organic carbon content was measured using a Costech elemental analyzer coupled to a Thermo MAT-253 isotope ratio mass spectrometer (Larson et al., 2008). Split samples were weighed into tin capsules, with

Table 3
Uranium, strontium, and thorium concentrations, total organic content, and uranium and strontium isotope compositions inferred from leachates of arkosic sandstone core samples obtained from the Smith Ranch–Highland mining unit-4 in Wyoming.

Laboratory ID	Core samples	Depth (m)	Leached U (mg/g core leached)	Leached Sr (mg/g core leached)	Leached Th (mg/g core leached)	Avg. % C
1	766-1	233.48	0.062761	0.025021	0.01223	3.12
2	766-2	233.63	0.111877	0.041597	0.007748	0.93
3	767-1	233.78	0.051499	0.020093	0.003548	1.56
4	769 dark	234.39	2.103842	0.0301	<0.007	7.73
5	769-1	234.48	0.162678	0.025878	0.005689	1.44
6	769-2	234.64	0.331585	0.035085	0.005117	0.63
7	770-1	234.70	1.383221	0.034241	0.005675	1.68
8	779 dark	237.59	24.84004	0.016958	0.001942	48.42
9	779-1	237.44	0.180231	0.033537	0.00352	1.32
10	779-2	237.65	15.99065	0.023436	0.004214	2.47
11	780-1	237.74	0.039502	0.018461	0.004686	0.40
12	782c	238.00	0.005393	0.014888	0.030954	0.38
13	782-2	238.51	0.004167	0.020809	0.00282	0.50
14	785-1	239.27	0.002712	0.013398	0.005466	0.49
16	786-1	239.57	0.011585	0.02017	0.014574	0.36

| Laboratory ID	Core samples	Depth (m)	$^{238}U/^{235}U$	$^{234}U/^{238}U$	$^{234}U/^{238}U$ activity ratio	$^{87}Sr/^{86}Sr$
1	766-1	233.48	137.6046	7.13E−05	1.485524694	0.712977
2	766-2	233.63	139.2778	6.30E−05	1.318984338	0.712637
# 3 (average)	767-1	233.78	137.82535	5.90404E−05	1.232217878	0.712207
#4 (average)	769 dark	234.39	137.4404	5.57014E−05	1.162536591	
5	769-1	234.48	137.8123	5.24E−05	1.095934479	0.715077
6	769-2	234.64	137.9235	6.13E−05	1.276408031	0.712986
#7 (average)	770-1	234.70	137.7119	5.62466E−05	1.175278394	
8	779 dark	237.59	137.8167	6.14E−05	1.278977457	
9	779-1	237.44	137.6551	4.44E−05	0.930505448	0.713196
#10 (average)	779-2	237.65	137.8904	6.21315E−05	1.298148564	
11	780-1	237.74	137.8443	4.80E−05	1.002305441	0.715211
#12 (average)	782c	238.00	137.997	3.47403E−05	0.725443587	0.71516
13	782-2	238.51	137.6441	3.67E−05	0.768016507	0.713475
14	785-1	239.27	137.7604	3.12E−05	0.652665251	0.713723
#16 (average)	786-1	239.57	137.79325	3.1169E−05	0.651701772	

mass spectrometer response calibrated to carbon content in elemental analysis standards (NIST 1547 Peach Leaves, NBS 2704 River Sediment, Eurovector BBOT, Eurovector Urea). The results of the organic carbon mass percentage are provided in Table 3 along with the corresponding mass fraction of uranium (g U/g) determined from the analysis of leachates described in Section 2.7.

2.6. Micro XRF elemental maps

A thin section of an organic-rich sample (779 dark) from the post-ISR mined ore zone was mounted on an EDX Eagle III instrument that was run at 40 kV, 400 μA. An area of the thin section (17 mm × 18 mm) was mapped at a step interval of 33 μm × 44 μm (Fig. 5). The dwell
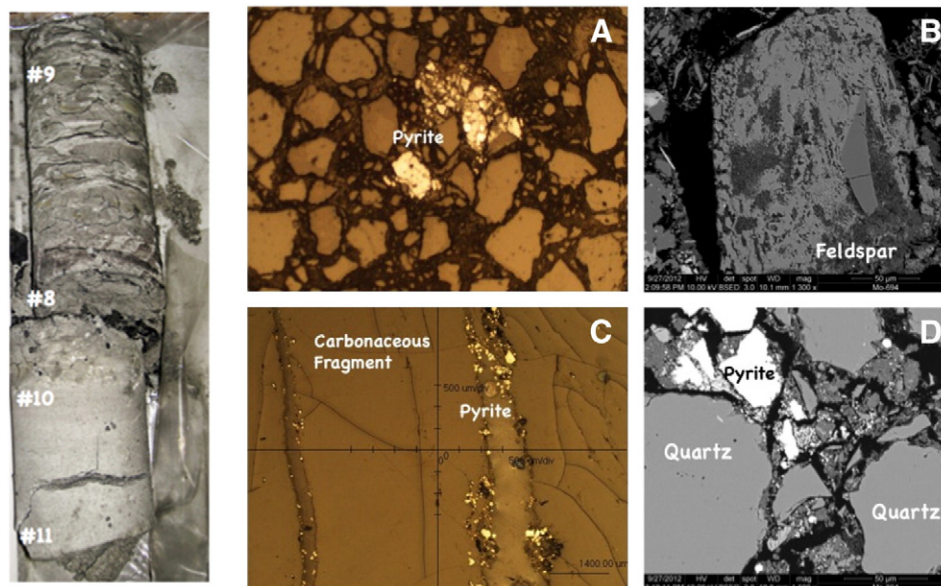
Fig. 2. A core with organic-rich (#8 and 9) and arkosic sandstone (#10 and 11) is shown on the left. Petrographic (A and C) and SEM (B and D) images of selected thin sections from organic-rich 769 dark (C) and organic-poor 782c (A, B, and D) of post-ISR-mined cores from MU-4 ore zone collected at depths of 237.6 m and 238.4 m, respectively.
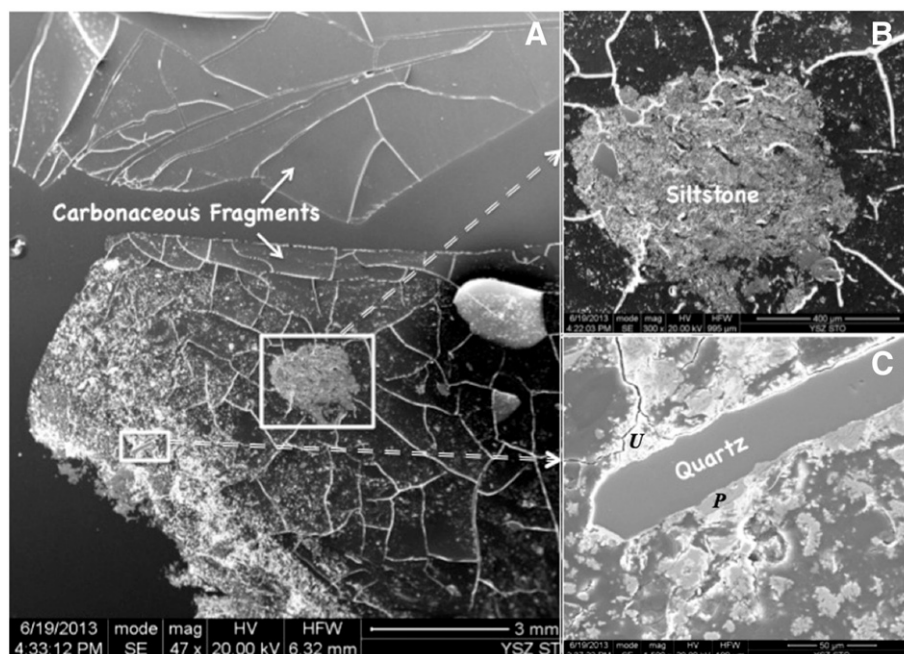
Fig. 3. SEM images of organic-rich 779 dark from MU-4 ore zone, showing considerable amounts of U (white) and pyrite (P, gray) crystallized on carbonaceous fragment fractures and matrix (A and C), rock fragment (B), and quartz grain (C).

time on each point was 200 ms and the run time was 19.6 h. Maps of U, Al, Fe, S, Ge and other trace elements distributions and concentrations within a carbonaceous fragment were recorded using a 10 μm per pixel resolution.

2.7. U and Sr isotope measurements of leachates from core fragments

Small fragments (0.07–0.7 g) taken from the post-ISR mined cores were leached using 4.5 mL of a 1.9 molar nitric acid with trace amounts of hydrogen peroxide to accelerate the dissolution of U. Aliquots of leachates were sent to the University of California (UC) Berkeley for U and Sr isotope measurements. U isotope ratios were determined using the GV Instruments IsoProbe MC-ICPMS located at Lawrence Berkeley National Laboratory (LBNL). The IsoProbe uses an Aridus II desolvation system to introduce samples in a 30 ppb solution. The isotopes ^{238}U and ^{235}U were measured on Faraday cups and the ^{234}U was measured on a Daly ion-counting system (Christensen et al., 2004). Estimated precision for ^{234}U/^{238}U activity ratios is <0.2% (2 sigma) and ^{238}U/^{235}U is 0.05% (1σ). ^{238}U/^{235}U ratios are reported in delta notation relative to bulk silicate earth (BSE), which is ^{238}U/^{235}U = 137.88. Solutions from the U isotope separations were evaporated to dryness and re-dissolved in 8 M HNO$_3$. Sr isotope ratios were measured on the Thermo Fisher Triton thermal ionization mass spectrometer (TIMS) located at UC Berkeley. Purified Sr was loaded onto zone-refined rhenium filaments using 1% phosphoric acid and a TaCl$_5$ activator solution. Sr isotope ratios were measured on Faraday cups using a static routine. Mass discrimination was corrected using ^{86}Sr/^{88}Sr = 0.1194. Isobaric interference from ^{87}Rb was monitored at ^{85}Rb and corrected when ^{87}Rb/^{86}Sr exceeded 10^{-5}. The Sr isotope standard NBS 987 was measured repeatedly during the study interval (n = 6) with a value of 0.710263 ± 0.000007 (2σ). This compares to the accepted value of 0.710245. The analytical results are given in Table 3 and selected results are plotted in Fig. 6.

2.8. XANES and EXAFS analyses and data collection

XANES and EXAFS data for bulk pyrite standard were collected at beam line 11-2 at the Stanford Synchrotron Radiation Light (SSRL) source (www-ssrl.slac.stanford.edu/content/beam-lines/beam-lines-by-number). The samples were pulverized in a regular hood and loaded

into an aluminum holder 1.b (http://www-group.slac.stanford.edu/esh/rp/fo/SSRLsampleholderscatalog.pdf). All μXANES, μEXAFS and μ-XRF data presented in the paper were collected on an organic-rich thin section (779 dark) at beam line 2-3. The preparation of thin sections is described in Section 2.1. The samples were run at room temperature and no precautions were taken to reduce potential oxidation of U during analysis. U-bearing samples are typically run at low temperature to minimize oxidation at the beam line. However, this capability was not available at beam line 2-3 for our sample type. Si(111) crystals were used to monochromate the incoming beam. The X-ray optics at beam line 2-3 focus the beam to a 2-μm spot. A single channel Ge detector for μXRF mapping and μEXAFS measurements was used. We calibrated the detector and set the windows to collect the fluorescence signal from elements of interest: U, Th, Ga, Fe, Zn, Zr, K, Ca, Ti, Mn, Cu, Se, Pb, Br and establish the element mapping analysis for elements with Z ≥ Ca. The recorded μXRF maps were analyzed using the microprobe analysis kit software package developed at SSRL. The EXAFS spectra were obtained in the fluorescence mode, at room temperature. The energies are calibrated by using the transmitted beam to measure the absorbance of Y foil (for U samples) measured prior to the sample measurement. Second-order polynomials are fit through both pre-edge and post-edge regions for normalization of the edge jump to unity. Several spots with the highest U and Fe counts were analyzed by taking multiple scans for each sample location (Figs. 7 and 9). The scans are averaged after interpolating the data for the individual scans. The smooth atomic absorption is approximated with a spline polynomial whose knot positions are adjusted to minimize the area of the modulus of the Fourier transform of the k^3-weighted EXAFS below R = 1–1.2 Å. Fourier transforms are calculated after the application of the sine window function to the EXAFS. Metrical parameters are obtained from the EXAFS weighted by k^3 via nonlinear, least-squared, k-space curve fits using the standard harmonic EXAFS equations summed over shells and amplitudes and phases obtained from code FEFF7. Uncertainties are obtained by calculating least square errors to the fit with and without the wave from a particular shell to determine its overall improvement in the quality of the fit and thin shifting the parameter until the fit is worse by 10% of this quantity. The number of relevant independent points for each fit was estimated using the following equation: $N_I = (2\delta k\delta R / \pi) + 2$ (Stern, 1993). The spatial correlations for the μXRF element maps are
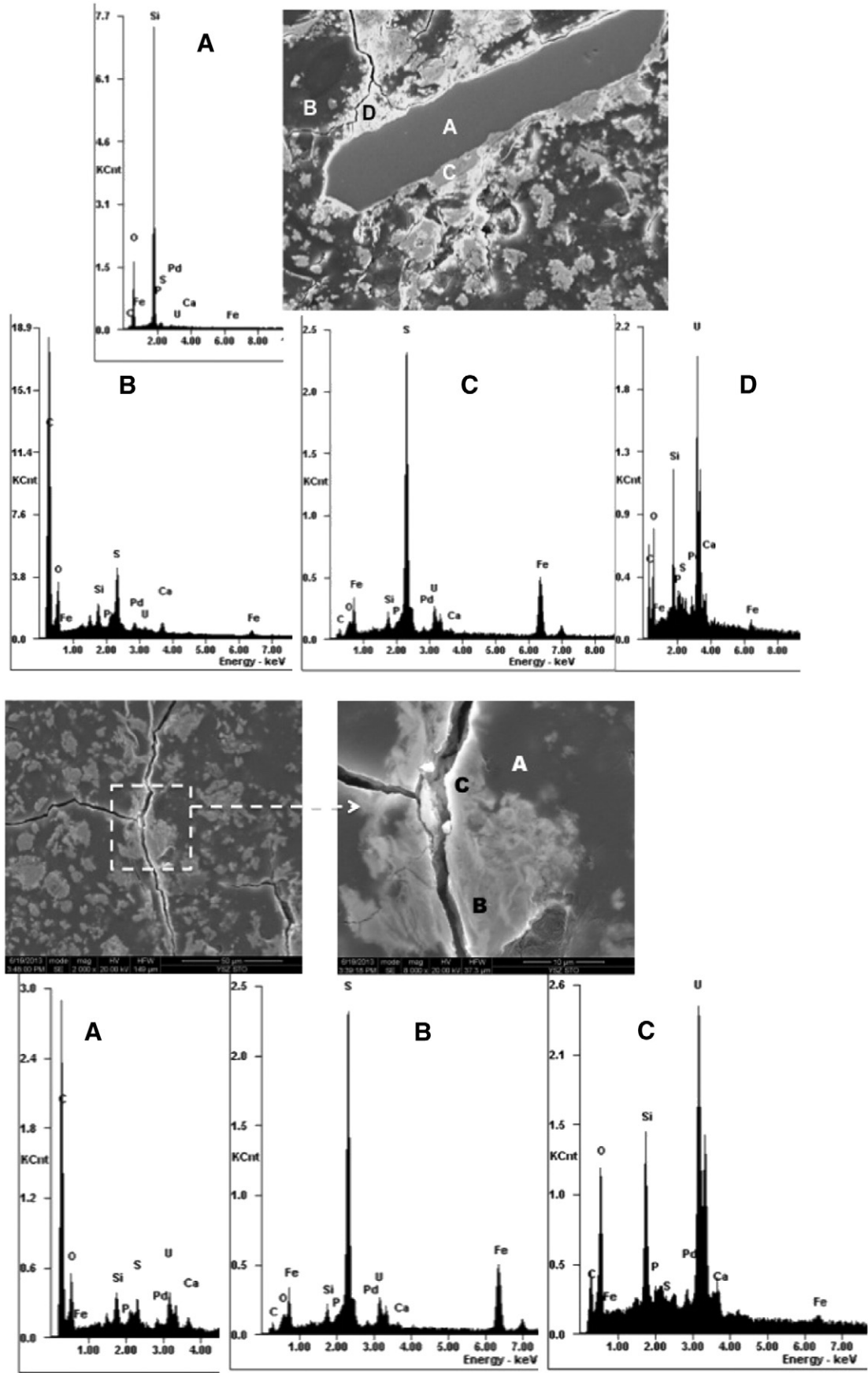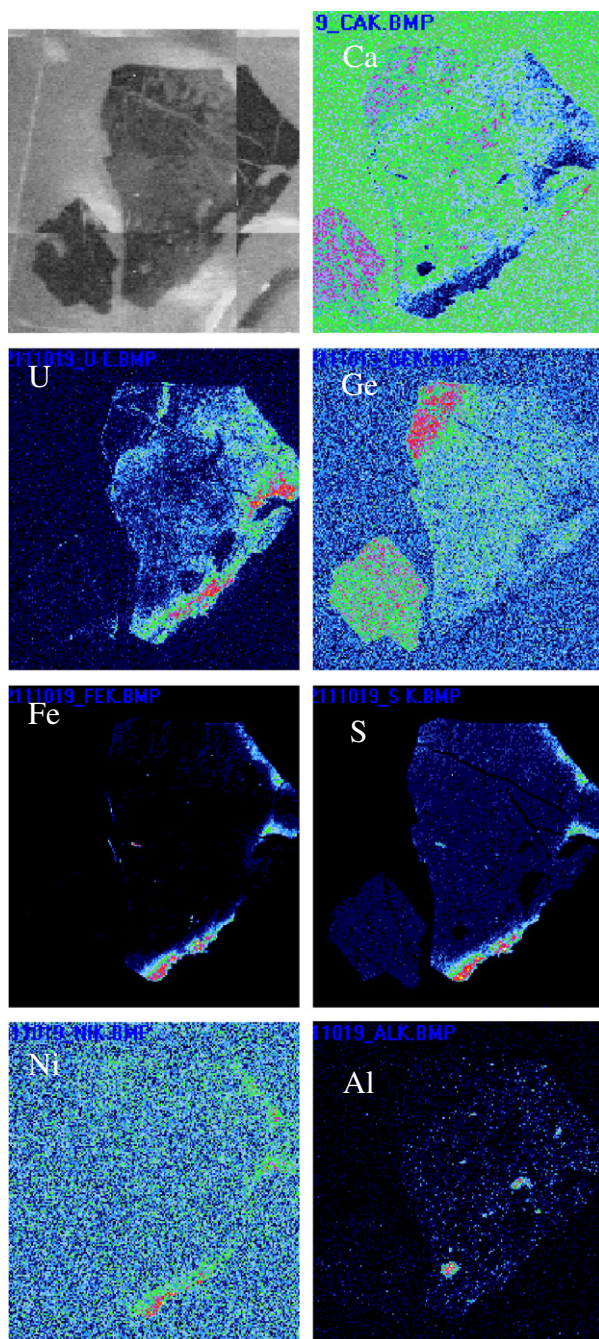
Fig. 5. μXRF elemental maps of trace metals of a thin section of a carbonaceous fragment (779 dark) recorded using a 10 μm per pixel resolution on sample that is a few centimeters large.

calculated using the Pearson function that measures the strength of association between a pair of variables. For the correlations between experimental data and the fitting results, the root mean square deviation was used. This function is frequently used as a measure of the differences between values predicted by a model or an estimator and the values actually observed from the data being modeled or estimated.

3. Results

3.1. Petrographic, mineralogical, and chemical characteristics of post-ISR mined cores

Sedimentary rocks with abundant detrital and diagenetic brittle minerals (e.g., quartz, feldspar, and carbonates), identified using petrographic and mineralogical methods generally have higher porosity (Chen et al., 2011). This is consistent with results from petrographic analyses of the ISR-mined cores that indicate moderately sorted and poorly consolidated arkosic sandstone, containing abundant quartz, feldspar, mica, carbonaceous fragments and minor clay minerals, biotite, iron oxide, pyrite, and traces of hornblende. The low clay mineral contents are probably related to insignificant alteration because of shallow burial. Most of the feldspars are coarse, fractured, and partially altered to clay minerals. Carbonaceous fragments of variable sizes commonly occur within the arkosic sandstone and their abundance varies with depth. Pyrite is sparsely disseminated and occurs within the clayey matrix, along the edges of minerals, and on surfaces and along fractures of carbonaceous fragments (Figs. 2–4).

In addition to petrographic observations, backscattered SEM images indicate abundant residual U and pyrite associated with carbonaceous matter, quartz, rock fragments, and fractures within organic-rich samples (Figs. 3 and 4). A fine-grained U-bearing mineral is the dominant phase because it coats and sometimes completely covers pyrite grains (Fig. 4A). U minerals are also dominant within fractures that probably acted as fluid pathways. Pyrite and U also occur within fractures and matrix of a rock fragment that is embedded within a larger carbonaceous fragment (Fig. 3B). The close association of U and pyrite as discontinuous patches on carbonaceous fragments, fractures, and along grain boundaries indicate that U postdates pyrite. Both minerals are partially altered, possibly during the ISR mining and pyrite appears to be responsible for the reductive immobilization of U. However, the U deposited on pyrite as indicated by SEM might only be a thin coating and only a small fraction of the total U. This seems to be the case in light of further analyses obtained by μXRF and μEXAFS, which are more penetrating.

The quantitative XRD results indicate the types and abundances of the detrital (i.e., quartz, K-feldspar, albite, mica, and carbonaceous fragments) and secondary (smectite, kaolinite, minor pyrite and calcite, and traces of coffinite) mineral contents of the post-ISR mined cores (Table 1). The results are consistent with the petrographic and SEM data. All core samples have similar detrital and secondary mineral contents even though some contain considerable amounts of carbonaceous matter, calcite, and pyrite. U content is mostly below detection limit of the X-ray diffraction analysis except for traces of coffinite in three of the organic-rich samples (Table 1).

The core samples were chemically analyzed by XRF to evaluate the effects of continuous circulation of oxidizing solutions on the host rocks during the ISR mining of MU-4 from 1999 to 2005. The post-mined samples from the ore zone are silica-rich (73–88 wt.%) but the rest of the major oxides make up less than 15 wt.% (Table 2). Despite a granitic origin, the K_2O, Na_2O, and Al_2O_3 contents are significantly depleted even though the petrographic and mineralogical results indicated abundant albite, K-feldspars, and clay minerals (Tables 1 and 2). The mafic oxide (e.g., CaO, Fe_2O_3, MgO, and TiO_2) contents are low, consistent with a granitic source for the sandstone. The major oxides also vary with depth. Some samples (779-1 and 779-2) contain higher concentrations of Al_2O_3, Fe_2O_3, TiO_2, MgO, and CaO, consistent with the mineralogical compositions of the samples (Table 1).

Fig. 4. SEM image of sample 779 dark (upper) shows a carbonaceous fragment and elongated quartz (A) that is coated with pyrite (C, gray) and U (D, white) on the upper and lower sides of the grain. EDAX patterns identify major mineral phases (i.e., A = quartz, B = organic matter, C = pyrite, and D = U and Si (coffinite from XRD analysis)). The lower SEM images of the same sample show fractured organic fragment (A), pyrite (B), and U (C) along fractures and on the surface of the carbonaceous material. The EDAX patterns identify the major mineral phases in the image (i.e., A = organic matter, B = pyrite, and C = U and Si (coffinite)).
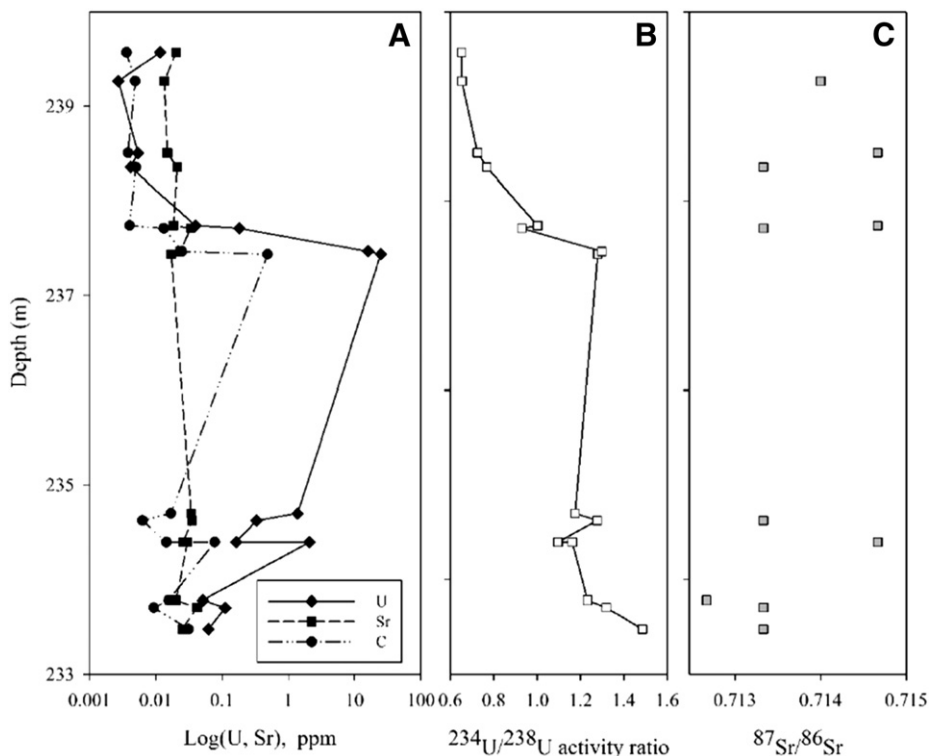
Fig. 6. Variations of uranium, strontium, and total organic carbon concentrations (A), $^{234}U/^{238}U$ activity ratios (B), and strontium isotopes (C) with depth.

Like the major oxides, the trace element contents indicate minor variations with depth. A few of the samples contain elevated concentrations of V, Ni, Ge, As, Rb, Zr, Nb, Pb, and U (Table 2). The U concentration increases with increased contents of Fe_2O_3, CaO, and P_2O_5 as well as with several trace elements (e.g., V, Ni, Ge, Rb, Ce, Nb, Pb, Zn, and Zr). Similar features are noted between U concentration and total organic carbon (TOC), loss on ignition (LOI), clay minerals, and pyrite contents (Tables 2 and 3). There is an apparent correlation between the elevated organic carbon content and elevated metal content consistent with the

capacity of the organic matter to complex and accumulate metals, including U.

Post-ISR-mined samples from the lower part of the core hole (237.7–239 m) generally contain slightly lower organic (<0.5 wt.%) and clay mineral (<6 wt.%) contents and low residual U concentrations (2.7 to 40 μg/g) unlike samples from the upper section (Tables 2 and 3). The uppermost (232.6–237.4 m) samples have higher organic matter (0.6 to 48 wt.%) and clay minerals (>6 wt.%) in most cases. The core samples contain variable amounts of carbonaceous fragments that are randomly
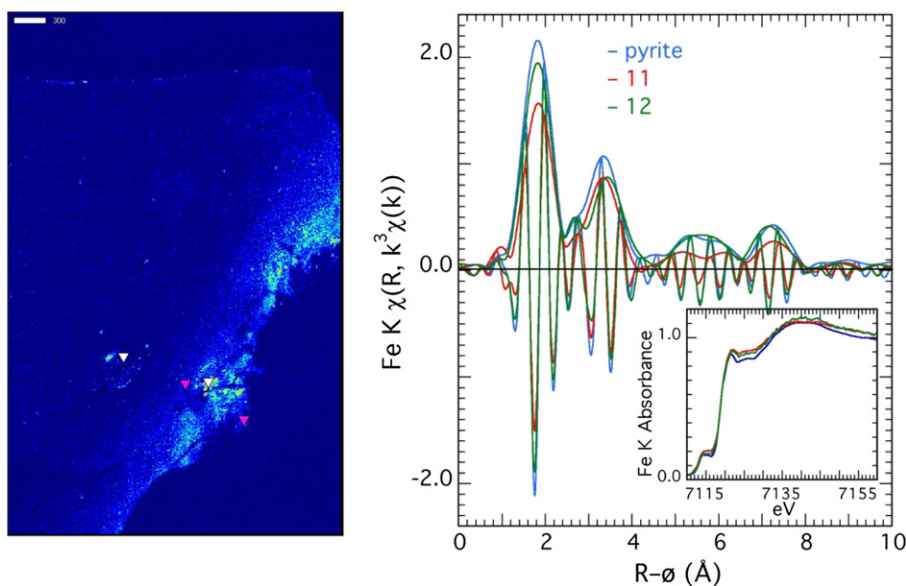

Fig. 7. Elemental maps of Fe for sample 779 dark (left) recorded using a 2 μm per pixel resolution on a sample that is a few centimeters in size; the maps were recorded at 17,500 eV with a dwell time of 50 ms at beam line 2-3. The scale bar represents 300 μm. Fe K-edge EXAFS and XANES spectra (shown on the right corner) were recorded at the white triangle areas, which show the highest Fe counts. The EXAFS and XANES spectra of pyrite were recorded at bean line 11-2 using a pure pyrite standard.

distributed within the arkosic sandstone except in a few cases where discrete layers of matted carbonaceous matter were noted (Fig. 2).

Leachates from core fragments are enriched in U compared with Sr and Th and are consistent with the results of the bulk chemical analysis (Tables 2 and 3). Both U and Sr generally decrease with depth like the trace element data from the bulk analysis (Fig. 6A). The low Th content and depletion of some of the major and trace elements are probably related to preferential loss of the elements during the ISR mining and possibly due to low solubility of Th in groundwater and the preferential migration of U from the source.

The $^{234}U/^{238}U$ activity ratios of the leachates show a range of values (0.650–1.486) that decrease with depth (Table 3, Fig. 6B). The core samples from the upper part of the section yielded elevated activity ratios and are correlated with higher U concentrations in those samples (Tables 2 and 3). Lower activity ratios suggest greater leaching during mining, as ^{234}U tends to be more easily dissolved and mobilized from U phases than ^{238}U because it is generally not as well incorporated into crystalline lattices due to alpha recoil during its formation from decay of ^{238}U (Ludwig, 1978; Pekala et al., 2010). Repeat analyses yielded consistent activity ratio results. The $^{87}Sr/^{86}Sr$ isotopic compositions of the leachates are highly variable and there is no discernible relationship with depth or other variables (Tables 2 and 3).

3.2. Elemental maps of U-bearing organic-rich sediments

The μXRF elemental maps indicate discrete zones with high concentrations of U, Ni, Fe, Ca, and S, and Ge along the edge of a carbonaceous fragment (Fig. 5). The Fe, Ni and S associations signify the abundance and co-location of iron and nickel sulfide minerals, but without apparent U association. The U-rich surfaces appear to be spatially separated from the high-Fe zones. Moreover, an isolated Ge-enriched zone is noted in a different part of the carbonaceous fragment. The μXRF elemental maps show poor correlation between the highest concentrations of Fe and U despite the close association of both minerals (i.e., U and pyrite) as shown in the SEM data (Figs. 3 and 4). These results suggest sequential formation of the Fe and U phases rather than concurrent formation.

3.3. EXAFS results of Fe and U

To gain an understanding of oxidation state distribution of Fe and U within the 779 dark sample, we performed EXAFS analyses on selected spots with the highest U and Fe concentrations. A pyrite standard was also analyzed at beam line 11-2 to determine the XANES and EXAFS spectra of pure pyrite. Fe K-edge XANES spectra recorded at two different locations with high Fe concentrations closely resemble the spectrum of a pure pyrite sample run at beam line 11-2 (Fig. 7 right inset). Also shown in Fig. 7 is the elemental map, with the Fe distribution and EXAFS spectra recorded at two areas of the sample along with the spectrum of the pure pyrite compound used as a reference material. The spectrum has a peak at around 7127 eV and a broad shoulder at 7140 eV. The close resemblance of the Fe spectrum in the sample with the spectrum of the pyrite indicates that Fe is present as Fe(II) in the
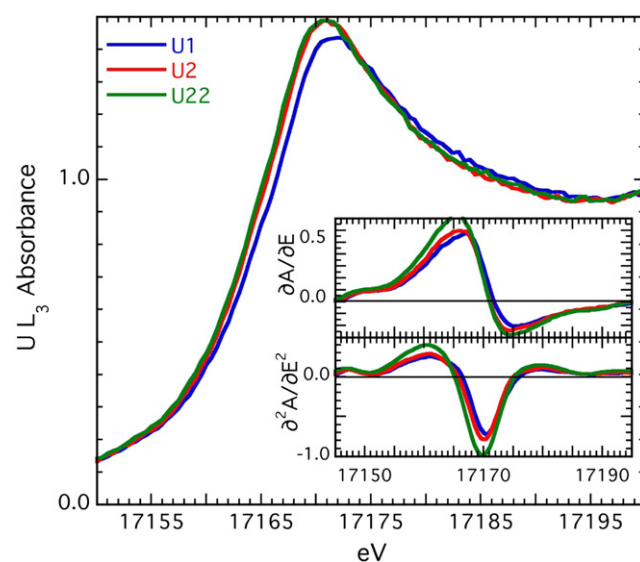

Fig. 8. U X-ray absorption near-edge structure (XANES) analysis for multiple locations within sample 779 dark. The first and second derivatives of the spectra are shown in the inset; lower right of the spectrum.

samples examined. The result is consistent with the EXAFS data, which show that the spectra of the sample and the pyrite standard are identical, and consistent with published data (Table 4, Fig. 7) (Finklea et al., 1976; Totir et al., 1997). Analysis of the inverse Fourier transform of the EXAFS shell yielded Fe–S and Fe–Fe distances that are identical to that determined from the crystal structure of pure pyrite. Thus, the EXAFS of the pyrite standard is well defined, whereas the amplitudes of the peaks from the EXAFS analyses of the geological samples are slightly lower because they are more disordered compared with a pure crystal. The EXAFS of the geological samples are almost perfectly aligned with that of the pyrite standard, confirming the presence of the same neighbor shells at equal distances (Fig. 7). The sample, pyrite standard, and the crystallographic data are summarized in Table 4.

U L_{III}-near-edge XANES spectra recorded at multiple locations of the 779 dark sample are presented in Fig. 8 and the U L_{III}-edge EXAFS and corresponding Fourier transform are presented in Fig. 9 along with the elemental maps, representing the distribution of U in the sample. The XANES spectra recorded at different locations are very similar and are characterized by a broad peak at about 17,172 eV and the absence of a shoulder at 17,190, which is observed in U(VI) compounds. The XANES spectra recorded for the 779 dark sample is consistent with the presence of U in a reduced form (U(IV)). However, the presence of small amounts of oxidized U ($\leq$10–20% UO_2^{2+}) cannot be excluded. Given the small amounts of potential U(VI) in the samples, the spectra were not analyzed to determine the percentage of U present in the oxidized U(VI) state. The U L_{III}-edge EXAFS representing an average of multiple spectra for one of the locations analyzed is presented in Fig. 9 along with the curve fitting and Fourier transforms of the EXAFS data. The metrical parameters of the fit and comparison with literature data

Table 4
Structural parameters for pure pyrite, iron in sample 779 dark and crystallographic data from the literature.

Specimen	Shell	Number of atoms	R, Å
Iron in 779 dark	Fe–S	7.5 ± 2	2.25 ± 0.02
	Fe–Fe	10.8 ± 3	3.76 ± 0.02
	Fe–S$_2$	6.2 ± 2	3.43 ± 0.02
Pyrite compound	Fe–S	11.6 ± 3	2.26 ± 0.01
	Fe–Fe	12.1 ± 3	3.79 ± 0.01
	Fe–S$_2$	6.2 ± 2	3.46 ± 0.02
Literature data	Fe–S	6	2.26 (Tryk et al., 1995; Brec et al. (1989); Wu et al. (2004))
	Fe–Fe	12	3.83
	Fe–S$_2$	4	3.62
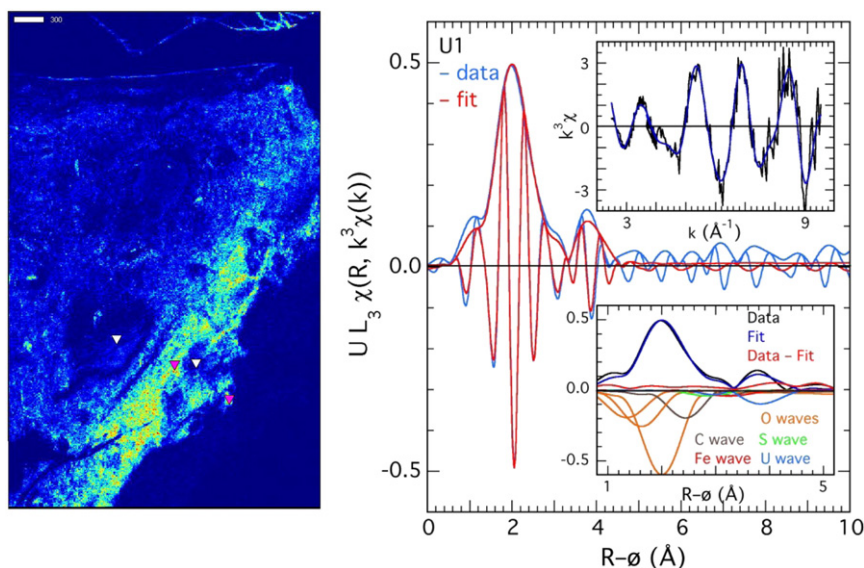
Fig. 9. Elemental maps of U for sample 779 dark (left) recorded using a 2 μm per pixel resolution on a sample that is a few centimeters large. The maps were recorded at 17,500 eV with a dwell time of 50 ms. The scale bar represents 300 μm. Representative U L_{III}-edge XAFS for one of the locations along with the fit and the different shells used to fit the data are represented.

are summarized in Table 5. The EXAFS data for the U from 779 dark are best modeled with 4.4 oxygen atoms at 2.44 Å, 0.85 atoms of oxygen at 1.79 Å, 2.90 atoms of carbon at 2.90 Å, and 1.3 atoms of oxygen at 2.06 Å. No U–U shell is needed and although a U–S shell at 3.26 Å and a U–Fe shell at 3.52 Å can be included in the fit, they do not further improve it (Gallegos et al., 2013). There is also no evidence for the presence of a Si shell at 2.8–3.8 R (Å). This is consistent with the absence of any U–Si correlation in the μXRF data (Fig. 5).

The fit parameters closely resemble the parameters for U(IV) triscarbonate, U(VI) tris carbonate complexes (Bargar et al., 1999; Wang et al., 2013), and U(VI) incorporated into calcite and aragonite (Reeder et al., 2000). The U–O distance of 2.44 Å determined for our sample which is the same as that determined for U(IV) triscarbonate complex [U(CO$_3$)$_3$(H$_2$O)$_2$]·2H$_2$O (Wang et al., 2013), is similar to the U–O distances determined for uranyl triscarbonate U(CO$_3$)$_3$(H$_2$O)$_2^{2-}$ of 2.40–2.49 Å (Bargar et al., 1999; Reeder et al., 2000), and within the range of U–O distances of 2.42–2.44 determined for U incorporated into aragonite (Reeder et al., 2000). In addition, the presence of 3 carbon atoms at a distance of 2.90 Å is consistent with U being in a form complexed with carbonate-like ligands. The U–C distance of 2.89–2.90 Å

are typical for U(IV) and U(VI) coordinated with three bidentate carbonate groups (Bargar et al., 1999; Reeder et al., 2000; Wang et al., 2010). The U–O distances for U(IV) and U(VI) triscarbonate complexes are very similar and it is difficult to distinguish between these forms based on the distances and number of coordinating atoms. However, given that U in our samples is present predominantly as U(IV) it is likely that the compounds analyzed represent U(IV) complexed with either simple U-carbonate like complexes or U(IV) complexed carboxylic acid type moieties. However, it is likely that some of the U might be present as U(VI) associated with carbonate. The lack of significant U–U contribution and the absence of any significant U–S, U–Fe, U–Si interactions (Gallegos et al., 2013; Wang et al., 2013) strongly suggests that U analyzed in these samples is predominantly present in a monomeric form. There is a small contribution of a U-oxo moiety observed at 1.79 Å, which indicates that U is partially oxidized and is possibly a U(VI)–carbonate complex or U(VI) incorporated into calcite. Some U(VI) that is complexed by organic matter and/or carbonate might also be present. There are no indications of the presence of any Fe(III) phases in the analyzed areas and no Fe–U interactions that would suggest that a fraction of the U is adsorbed onto oxidized iron phases. The

Table 5

Structural parameters for a natural uranium sample obtained from a carbonaceous ore sample and structural parameters from other uranium compounds from the literature for comparison.

Compound	Coordination shell	Number of atoms	Type of atom	R, Å	Reference
Current data					
Current sample	U–O	4.3 ± 1	O	2.44 ± 0.02	
Current sample	U═O	0.8 ± 0.3	O	1.79 ± 0.01	
Current sample	U–C	2.9 ± 1	C	2.91 ± 0.02	
Current sample	U–O	1.3 ± 1	O	2.06 ± 0.01	
Literature data					
Schoepite	U–O		O	1.81	Aamrani et al. (2007)
U(VI) adsorbed onto ferrihydrite	U═O		O	1.78–1.81	Reich et al. (1998)
U(VI) adsorbed onto hematite	U═O		O	1.79–1.82	Totir et al. (1997), Bargar et al. (1999)
U(VI) adsorbed onto goethite	U═O		O	1.76–1.80	
U(VI) adsorbed onto ferrihydrite	U–O		O	2.35–2.52	Reich et al. (1998)
UO$_2$	U–O	8	O	2.35	Aamrani et al. (2007)
Schoepite	U–O	3.3	O	2.31	Aamrani et al. (2007)
	U–O	0.8	O	2.55	Aamrani et al. (2007)
UO$_2$(CO$_3$)$_3^{4-}$ (aq)	U–C	3	C	2.88	Bargar et al. (1999)
	U–O	8.7	O	2.43	Bargar et al. (1999)
U(CO$_3$)$_3$(H$_2$O)$_2$	U–O	6	O	2.39–2.49	Wang et al. (2010)
	U–C	3	C	2.82	Wang et al. (2010)
	U–O	2	O	2.225	Wang et al. (2010)

absence of shorter U–O distances in the order of 2.32–2.38 Å generally reported for U and uranyl species adsorbed onto iron phases suggests that the U analyzed in our samples is not an adsorbed uranyl carbonate species (Bargar et al., 1999; Livens et al., 2002). The observation of some unusual U–O short distances at 2.06 Å might suggest the presence of some other U phases such as species that possess bridging oxo ligands (Walter et al., 2003).

4. Discussion

Petrographic, mineralogical, and chemical data collected from core samples provided valuable information for assessing the sedimentological and burial diagenetic processes that led to the formation of the sandstone-type U roll-front deposits within arkosic sandstone host rocks. Information about the burial diagenetic processes and the resulting secondary mineral assemblage are relevant both for developing effective ISR mining techniques and to understand post-mining geochemical conditions that could result in downgradient migration of residual fluids and chemicals related to ISR mining. The geological processes and post-ISR mineralogical and chemical features are highlighted next.

4.1. U ores and burial diagenetic processes

The U ore deposits at the Smith Ranch–Highland location were derived from the weathering of granitic source rocks located along the southern margin of the Powder River Basin and from the alteration and leaching of granitic sediments and late Tertiary volcanic ashes deposited within the basin consistent with the origin of the arkosic sandstone host rocks (Seeland, 1976; Santos, 1981; Flores et al., 1999; Freeman and Stover, 1999). The absence of mafic minerals within the arkosic sandstone confirms that the sediments were derived primarily from granitic rocks. U was presumably mobilized by oxygenated and carbonated waters and appears to have been immobilized when it encountered reducing conditions within or near carbonaceous matter and pyrite, which are commonly present at variable amounts within the arkosic sandstone. The primary and secondary mineral assemblages suggest that the shallow burial diagenetic processes were not intense, consistent with the insignificant alteration of the detrital minerals and the lack of cementation within the matrix of the host rocks, thus allowing fluids to readily flow during the formation of the roll-front deposits.

Quartz exhibits traces of overgrowth along rounded and subrounded grain boundaries, whereas feldspars (e.g., K-feldspar, and albite) are variably altered. The secondary minerals (smectite, kaolinite, pyrite, calcite, and trace amounts of coffinite), which are typical of low-temperature diagenetic alteration, represent at least 15 wt.% of the mineral assemblage. The mineralogical results are generally similar to published data from the Smith Ranch–Highland ore deposits (Seeland, 1976; Stewart et al., 2000; Heinrich, 2012). However, no minerals typical of high-temperature alteration processes (e.g., illitic clays) were noted. The presence of abundant smectite and poorly matured carbonaceous matter within the U-bearing arkosic sandstone provides additional evidence for the low-temperature environment during shallow burial diagenesis and deposition of U. This is also reflected in the abundance of detrital minerals and associated carbonaceous fragments compared with the minor fraction of secondary minerals present within the arkosic sandstone because of limited alteration during the low-temperature burial diagenesis. As a result, the arkosic sandstone units were poorly cemented and contained abundant void spaces, which subsequently allowed the influx and mobilization of mineralized fluids to form the U ore zones along the interface of a shallow redox front (Ludwig, 1978).

The K-feldspar and albite minerals indicate partial alteration and are closely associated with variable amounts of smectite and kaolinite. The overall clay mineral content is lower in the deeper samples (Table 1). Kaolinite is considerably less abundant and shows minor variation with depth compared with smectite. Both smectite and kaolinite appear

to have formed in situ from the alteration of K-feldspar and albite because of their close association with partially to totally altered feldspar grains. It is very unlikely that the partially altered feldspar grains were transported from the granitic mountains that surround the Powder River Basin because of strong hydrodynamic processes during fluvial transport. Thus, the abundance of smectite compared with kaolinite and the absence of mixed layer illite/smectite suggest that the early Tertiary arkosic sandstone host rocks were deposited in a shallow depositional environment and underwent minimum low-temperature alteration in the basin. Moreover, the poorly consolidated carbonaceous fragments, containing well-preserved plant structures, represent a low-grade peat deposit that is consistent with minimum thermal diagenesis.

4.2. Mineralogical features of post-ISR mined arkosic sandstone units

The core samples were obtained from post-mined deposits, and presumably most of the U was removed during the ISR mining. However, there is good evidence of poor contact between the mining lixiviant and U (coffinite)-bearing sandstone in some zones of the cored interval, particularly where organic carbon and clay mineral contents of the core are high. The sediments in the organic-rich areas (e.g., in the vicinity of the 779 dark sample) were still grayish in color rather than the yellow-orange color that is typical of oxidized sediments.

In the post-mined core samples, the abundance of U, Fe, and other metals closely associated with carbonaceous fragments suggests that the well-preserved plant remains have high affinity for metal binding (Fig. 5). For example, high Ge accumulation in carbonaceous materials is due to its strong affinity for organic matter rich in metal binding groups (Du et al., 2009; Li et al., 2011). The persistence of zones with high Fe, Ge, Ca, and U indicates a strong and non-specific affinity of the organic matter for metal complexation. Thus, organic matter within the arkosic sandstone played an important role in the concentration of U and other metals during the formation of the roll-front U ore zones. As shown in the SEM images in Figs. 3 and 4, the growth of U on pyrite is consistent with pyrite's known ability to immobilize U, which is probably present as a coating on the Fe-sulfide crystals (Hua and Deng, 2008; Bi and Hayes, 2014; Lee et al., 2014). However, the µXRF elemental maps indicate discrete areas in which the U-rich zones on the carbonaceous fragments have minimum overlap with other metals including Fe (Fig. 5). The pyrite is partially and/or totally armored with U, thereby somewhat concealing Fe and S. U associated with organic matter seems to be more abundant and might be present in thicker deposits. U associated with pyrite is likely present as a very thin coating or film. EXAFS analyses on select areas with the highest U and Fe concentrations provide information about the oxidation state distribution of Fe and U within the samples.

The persistence of U and Fe in the post-mined cores suggests a poor sweep of these areas with abundant carbonaceous fragments by the lixiviant solutions, which would be consistent with the hydrophobic nature of organic matter and the general association of the organic matter with finer-grained sediments in the core. U was not noted within the matrix of organic-poor sections of core, presumably because these were efficiently swept during ISR mining. These interpretations are in part consistent with the structural determinations performed by EXAFS in which most of the U found in our samples consisted of U(IV) complexed by carboxylate moieties. Addition of Fe–U and U–S does not enhance the numerical fit of the data. A Si shell at 2.8–3.8 R (Å) was not included in the fit for lack of any Si–U correlation in the µXRF data, which indicates that U and Si were not correlated. However, the presence of some U(VI) and unusual U–O distance suggests that more complex and ill-defined U forms are also present in the sample.

4.3. Geochemical features of post-ISR mined cores

The arkosic sandstone host rocks at the Smith Ranch–Highland U deposits indicate minor variations in chemical compositions with depth.

Comparisons of the results of samples from the upper (766-1 to 779-2) and lower (780-1 to 786-1) parts of the cores indicate distinct variations in major element contents (*e.g.*, SiO_2, Al_2O_3, Fe_2O_3, and CaO), LOI, and total organic carbon contents (Tables 2 and 3). Samples with lower LOI and lower total organic carbon have relatively higher SiO_2 and Na_2O but slightly reduced Al_2O_3, Fe_2O_3, and CaO. Clearly the depletions and slight enrichments are attributed to the ISR mining. Basically, samples containing abundant carbonaceous fragments and elevated U and pyrite from the shallow section of the mining unit were not significantly affected during the ISR mining, whereas the opposite is true with samples from the lower half of the section. The samples are variably hydrated (LOI = 1.3–15.7 wt.%) with depth. The loss on ignition (LOI) values, which depict the amount of volatiles (*i.e.*, water and gases) clearly map out the distributions and abundances of carbonaceous matter and clay contents of the core samples. A strong correlation is noted between high LOI values and the amount of total organic content (TOC) as well as higher concentrations of U, pyrite, and smectite (Tables 2 and 3). The LOI and chemical compositions from the XRF and leachate analyses of the core samples also indicate similar variations in U contents with depth (Tables 2 and 3).

Data from U and Sr isotopic analyses indicate additional characteristic features about the origin of the host rocks and associated U ores (Fig. 6). The deeper cores obtained from the post-ISR mined samples reveal a $^{234}U/^{238}U$ activity ratio that is characteristic of strong weathering (Lowson, 2013) or ISR leaching (Placzek et al., 2014, submitted to Economic Geology) that leads to the depletion of ^{234}U in solid phase ($^{234}U/^{238}U$ <1). However, samples from the upper half of the mined zone rich in carbonaceous materials contain U with a $^{234}U/^{238}U$ activity ratio above unity, which is consistent with insignificant ISR fluid–rock interaction in the aquifer and accumulation of U enriched in ^{234}U. Previous investigations reported that preferential loss of radioactive daughters was responsible for the younger and discordant apparent ages obtained during U–Pb dating of U ore bodies at the Highland mining unit (Santos and Ludwig, 1983). The presence of high concentrations of unsupported radiogenic daughters in pyrite and organic fragments is consistent with the selective migration of decay products from the U ore zones in Wyoming (Ludwig, 1978).

The core samples yielded high $^{87}Sr/^{86}Sr$ isotopic ratios (>0.712) that vary with depth (Fig. 6C). The similarity in isotopic compositions of most of the core samples probably signifies equilibration or minor isotopic exchanges between fluids and host rocks in the depositional environment. The results are within the range of isotopic values (>0.71) of Precambrian granitic rocks and alluvial sands derived from those rocks (Capo et al., 1998). The Sr isotopic ratios confirm that the arkosic sandstone units were derived from Precambrian granitic rocks that bound the southern portion of the Powder River Basin.

4.4. Implication to post-ISR contamination downstream from ISR-mined site

Our data show that the ore zone which is rich in residual uranium is also rich in carbonaceous matter and clay minerals. This is indicative of either a significant retardation of the effect of the leaching fluids or, more likely, a result of inefficient sweep of the sediment by the ISR fluids. In contrast, core fragments that contain low organic matter and clay minerals are depleted in their U contents. Pre-mining gamma logs of the core hole indicate high peaks around 234.7-m depth (organic-rich sample 770-1) and around 237.7-m depth (organic-poor sample 780-1) with a sharp drop below that. For example, 770-1 contains a significant amount of U compared with 780-1, consistent with more efficient leaching of U from the organic-poor zone (780-1) during ISR mining (Table 3). The organic-poor arkosic sandstone also had a much more oxidized yellow-orange appearance than the gray-black organic-rich rocks, indicative of extensive oxidation even though petrographic examination indicated a few grains of pyrite in one of the deeper samples.

The results of U isotope analysis indicate elevated $^{234}U/^{238}U$ activity ratios in the upper half of the ore zone, which gradually decreased with depth to below the secular equilibrium in uranium depleted areas (Fig. 6). Less than unity activity ratios have been related to strong natural leaching of U in weathering zones of U ores and to ISR leaching process (Walter et al., 2003; Placzek et al., 2014, submitted to Economic Geology). These observations are consistent with a greater degree of sweep and leaching of U in the deeper organic-poor ore zones at MU-4 that are consistent with lower (0.65–1.0) activity ratios.

The arkosic sandstone host rocks from the ore zone are poorly cemented and full of void spaces and access of leaching fluids does not appear to be an issue except for the organic-rich sediments, which are hydrophobic and contain more smectite that probably reduced the porosity of the arkosic sandstone.

The study indicates that ore zones rich in carbonaceous materials have lower porosity and increased hydrophobicity and were least affected by ISR mining fluids and therefore may provide little post-mining restorative benefit. These zones contain considerable U in a reduced form probably complexed to organic matter. This U is likely to be stable and might not contribute significantly to post-mining migration of U. In contrast, the lower part of the ore zone that contains trace amounts of organic matter and pyrite was subjected to considerable water–rock interaction where pyrite appears to be partially altered. This zone might provide some U attenuation through reductive deposition on partially altered pyrite. Residual pyrite may play a role in *in-situ* immobilization of U in the post-mined unit. However, more work is needed to determine the long-term stability of U reduced on the surface of iron sulfide minerals, which act as oxygen scavengers and might prevent U reoxidation (Bi and Hayes, 2014).

5. Conclusion

The integrated petrographic, mineralogical, and structural information gained by analyzing core fragments from a previously mined U ore zone provide significant insight into the sedimentological and burial diagenetic processes of the host rocks, the nature of the ore zones, and the factors that influence ISR mining and the fate and transport of contaminants downgradient of the mined unit. Our data suggest that carbonaceous materials which are abundant in the arkosic sandstone host rocks might have played a significant role in accumulating U and continue to act as a significant reservoir for U and other trace metals. U associated with the carbonaceous materials appears to be present predominantly as U(IV)-carboxylate complexes. The U (coffinite) associated with organic matter seems to either resist oxidation or more likely remained inaccessible to leaching fluids. Although these areas retained significant U and an important reducing capacity, they might not contribute significantly to U attenuation because they are likely disconnected from the main hydraulic flow system.

Trace amounts of pyrite were noted in post-mined cores that are significantly depleted in U contents consistent with extensive leaching during ISR mining. There is also some evidence suggesting reduction of U on the surface of pyrite in areas accessible to fluid flow. Residual pyrite in these swept zones might have acted as a reducing phase to partially attenuate U. More detailed investigations are needed to determine the nature of the U phases and their long-term stability.

References

Aamrani, S.E., Gimenez, J., Rovira, M., Seco, F., Grive, M., Bruno, J., Duro, L., de Pablo, J.A., 2007. Spectroscopic study of uranium(VI) interaction with magnetite. Appl. Surf. Sci. 253 (21), 8794–8797.

Bargar, J.R., Reitmeyer, R., Davis, J.A., 1999. Spectroscopic confirmation of uranium(VI)–carbonato adsorption complexes on hematite. Environ. Sci. Technol. 33 (14), 2481–2484.

Bi, Y., Hayes, K.F., 2014. Nano-FeS inhibits UO_2 reoxidation under varied oxic conditions. Environ. Sci. Technol. 48, 632–640.

Brec, R., Rouzet, E., Ouvrard, G., 1989. Redox processes in the Li_xFeS_2/Li electrochemical system studied through crystal, Mössbauer, and EXAFS analyses. J. Power Sources 26 (3–4), 325–332.

Capo, R.C., Stewart, B.W., Chadwick, O.A., 1998. Strontium isotopes as tracers of ecosystem processes: theory and methods. Geoderma 82, 197–225.

Chen, S., Zhu, Y., Wang, H., Liu, H., Wei, W., Fang, J., 2011. Shale gas reservoir characterization: a typical case in the southern Sichuan Basin of China. Energy 36, 6609–6616.

Chipera, S.J., Bish, D.L., 2002. FULLPAT: a full-pattern quantitative analysis program for X-ray powder diffraction using measured and calculated patterns. J. Appl. Crystallogr. 35, 744–749.

Christensen, J.N., Dresel, P.E., Conrad, M.E., Maher, K., DePaolo, D.J., 2004. Identifying the sources of subsurface contamination at the Hanford Site in Washington using high-precision uranium isotopic measurements. Environ. Sci. Tech. 38, 3330–3337.

Dahlkamp, F.J., 1993. Uranium Ore Deposits. Springer-Verlag, Berlin, Germany.

Du, G., Zhuang, X.G., Querol, X., Izquierdo, M., Alastuey, A., Moreno, T., Font, O., 2009. Ge distribution in the Wulantuga high-germanium coal deposit in the Shengli coalfield, Inner Mongolia, northeastern China. Int. J. Coal Geol. 78, 16–26.

Finklea III, S.L., Cathey, L.C., Amma, E.L., 1976. Investigation of the bonding mechanism in pyrite using the Mössbauer effect and X-ray crystallography. Acta Crystallogr. A32, 529–737.

Flores, R.M., Ochs, A.M., Bader, L.R., Johnson, R.C., Vogler, D., 1999. Framework geology of the Fort Union coal in the eastern Rock Springs uplift, Greater Green River Basin, Wyoming. US Geological Survey Professional Paper 1625-A, pp. GF-1–GF-14.

Freeman, M.D., Stover, D.E., 1999. The Smith Ranch Project: a 1990s in situ uranium mine. The Uranium Institute 24th Annual Symposium, 8–10 September, pp. 1–20.

Gallegos, T.J., Fuller, C.C., Webb, S.M., Betterton, W., 2013. Uranium(VI) interactions with mackinawite in the presence and absence of bicarbonate and oxygen. Environ. Sci. Technol. 47, 7357–7364.

Govindaraju, K., 1994. Compilation of working values and sample description for 383 geostandards. Geostand. Newslett. 18, 15–35.

Hall, S., 2009. Groundwater restoration at uranium in-situ recovery mines, south Texas coastal plain. U.S. Geological Survey Open-File Report 2009-1143 (32 p.).

Heinrich, G., 2012. Mineralogy of selected Smith Ranch–Highland in-situ recovery ores. Project No. 201097; Report No. TN 12-12. Cameco Technology and Innovation Research Center, pp. 1–46.

Hu, K.G., Wang, Q.L., Tao, G.Q., Wang, A.H., Ding, D.X., 2011. Experimental study on restoration of polluted groundwater from in situ leaching uranium mining with sulfate reducing bacteria and ZVI-SRB. The Second International Conference on Mining Engineering and Metallurgical Technology Book Series. Procedia Earth and Planetary Science 2, pp. 150–155.

Hua, B., Deng, B.L., 2008. Reductive immobilization of uranium(VI) by amorphous iron sulfide. Environ. Sci. Technol. 42, 8703–8708.

Larson, T.E., Heikoop, J.M., Perkins, G., Chipera, S.J., Hess, M.A., 2008. Pretreatment technique for siderite removal for organic carbon isotope and C:N ratio analysis in geological samples. Rapid Commun. Mass Spectrom. 22, 1–8.

Lee, S.Y., Cha, W.S., Kim, Jong-Gu., Baik, Min Hoon, Jung, Euo Chang, Jeong, Jong Tae, Kim, K., Chung, S.Y., Lee, Y.J., 2014. Uranium(IV) remobilization under sulfate reducing conditions. Chem. Geol. 370, 40–48.

Li, J., Zhuang, X.G., Querol, X., 2011. Trace element affinities in two high-Ge coals from China. Fuel 90, 240–247.

Livens, F.R., Jones, M.J., Hynes, A.J., Charnock, J.M., Mosselmans, J.F.W., Hennig, C., Steele, H., Collison, D., Vaughan, D.J., Pattrick, R.A.D., Reed, W.A., Moyes, L.N., 2002. X-ray absorption spectroscopy studies of reactions of technetium, uranium and neptunium with mackinawite. J. Environ. Radioact. 74, 211–219.

Lowson, R.T., 2013. $^{234}U/^{238}U$ signatures associated with uranium ore bodies: part 3 Koongarra. J. Environ. Radioact. 118, 163–168.

Ludwig, K.R., 1978. Uranium-daughter migration and U/Pb isotope apparent ages of uranium ores, Shirley Basin, Wyoming. Econ. Geol. 73, 29–49.

Luo, I., Weber, F.A., Cirpka, O.A., et al., 2007. Modeling in-situ uranium(VI) bioreduction by sulfate-reducing bacteria. J. Contam. Hydrol. 92, 129–148.

Mays, W.M., 1994. Restoration of groundwater at three in-situ mines in Texas. IAEA Technical Committee Meeting, Vienna Austria, Oct. 5–8, 1992 as reviewed in Nuexco Review, May 1994. Groundwater Restoration of In-Situ Uranium Mines.

Miller, C., Knode, R., Collings, S., 1990. In situ uranium mining extractive metallurgy at the Crown Butte Uranium Project. The Extractive Metallurgy Chapter of Denver, Denver, Co, USA, March 1990.

Norris, J.D., Drummond, P., 2000. Uranium recovery by in-situ leaching: the Smith Ranch project. Uranium 2000 — Processes Metallurgy of Uranium, pp. 311–319.

Pekala, M., Kramers, J.D., Waber, H.N., 2010. 234U/238U activity ratio disequilibrium technique for studying uranium mobility in the Opalinus Clay at Mont Terri, Switzerland. Appl. Radiat. Isot. 68, 984–992.

Placzek, C.J., Heikoop, J.M., House, B., Linhoff, B.S., Pelizza, M., 2014. Uranium isotope composition of waters from south Texas uranium ore deposits. Econ. Geol. (submitted for publication).

Reeder, R.J., Nugent, M., Lamble, G.M., Tait, C.D., Morris, D., 2000. Uranyl incorporation into calcite and aragonite: XAFS and luminescence studies. Environ. Sci. Technol. 34 (4), 638–644.

Reich, T., Moll, H., Arnold, T., Denecke, M.A., Hennig, C., Geipel, G., Bernhard, G., Nitsche, H., Allen, P.G., Bucher, J.J., Edelstein, N.M., Shuh, D.K., 1998. An EXAFS study of uranium(VI) sorption onto silica gel and ferrihydrite. J. Electron Spectrosc. Relat. Phenom. 96, 237–243.

Reimann, L., Huffman, L., 2005. Biological reduction of metals during ground water restoration presented at the Global Uranium Symposium. Casper, Wyoming (July 13).

Rigaku Corporation, 2009. ZSX Primus Series Instruction Manual.

Santos, E.S., 1981. Facies distribution in uranium host rocks of the southern Powder River Basin, Wyoming. U.S. Geological Survey Open-File Report 91-741, p. 15.

Santos, E.S., Ludwig, K.R., 1983. Age of uranium mineralization at the Highland mine, Powder River Basin, Wyoming, as indicated by U–Pb isotope analysis. Econ. Geol. 78, 498–501.

Seeland, D.A., 1976. Relationship between early Tertiary sedimentation patterns and uranium mineralization in the Powder River basin, Wyoming. Geology and Energy Resources of the Powder River. Wyoming Geol. Assoc., Ann. Field Conf., 28th Guidebook, pp. 53–64.

Stern, E.A., 1993. Number of relevant independent points in x-ray-absorption fine-structure spectra. Phys. Rev. B 48, 9825–9827.

Stewart, C.L., Reimann, L.J., Swapp, S.M., 2000. Mineralogic considerations for uranium in situ leach mining: a preliminary study of uranium and associated mineralogy of roll-front uranium deposits in Wyoming and Nebraska. Can. Inst. Min. Bull. 93, 89–96.

Totir, D.A., Bae, I.T., Hu, Y., Antonio, M.R., Stan, M.A., Scherson, D.A., 1997. In situ Fe K-edge X-ray absorption fine structure of a pyrite electrode in a Li/polyethylene oxide (LiClO₄)/FeS₂ battery environment. J. Phys. Chem. 101, 9751–9756.

Tryk, D.A., Kim, S.H., Hu, Y.N., et al., 1995. Electrochemical insertion of lithium into pyrite from nonaqueous electrolytes at room temperature — an in-situ Fe K-edge X-ray-absorption fine-structure study. J. Phys. Chem. 99, 3732–3735.

Walter, M., Arnold, T., Reich, T., Bernhard, G., 2003. Sorption of uranium(VI) onto ferric oxides in sulfate-rich acid waters. Environ. Sci. Technol. 37, 2898–2904.

Wang, J., Lu, X., Li, Z., Zhang, S., Cheng, S., 2010. Synthesis and crystal structure of a uranyl containing complex [U(CO₃)₃(H₂O)₂] 2H₂O. Chin. J. Inorg. Chem. 26, 351–354.

Wang, Y., Frutschi, M., Suvorova, E., Phrommavanh, V., Descostes, M., Osman, A.A.A., Geipel, G., Bernier-Latmani, R., 2013. Mobile uranium(IV)-bearing colloids in a mining-impacted wetland. Nat. Commun. 4, 1–9.

Wu, R., Zheng, Y.F., Zhang, X.G., Sun, Y.F., Xu, J.B., Jian, J.K., 2004. Hydrothermal synthesis and crystal structure of pyrite. J. Cryst. Growth 266 (4), 523–527.

Yi, Z.J., Lian, B., Yang, Y.Q., Zou, J.L., 2009. Treatment of simulated wastewater from in situ leaching uranium mining by zero valent iron and sulfate reducing bacteria. Trans. Nonferrous Met. Soc. China 19, S840–S844.